Laboratory Study of Polarized Scattering by Surface Waves at Grazing Incidence: Part I—Wind Waves

Anatol D. Rozenberg, Derek C. Quigley, and W. Kendall Melville

Abstract— **Laboratory measurements of Ku-band scattering at grazing incidence are presented. This study was motivated by the need to understand the processes which significantly contribute to scattering at grazing incidence. A dual polarized (VV, HH) coherent pulsed Ku-band scatterometer with good temporal resolution (3 ns) was used to obtain Doppler spectra and the absolute cross-section of scattered signals for grazing angles from 6–12°, and winds in the range 2–12 m/s. Wire wave gauges were used to measure the wind-wave field. Measurements of the first few moments of the Doppler spectra (cross-section, central frequency and bandwidth) showed that the data separated into two groups. The first grouping corresponded to HH scattering in the upwind look direction, and was clearly associated with scattering from the dominant gravity wind-waves. The second grouping corresponded to HH scattering in the downwind look direction, and all VV scattering, and was consistent with Bragg scattering from free higher frequency waves. This classification of the electromagnetic scattering was consistent with comparisons of direct and Doppler measurements of the kinematics of the surface wave field. The electromagnetic classification was also consistent with asymmetries in the wave field which increased with increasing wind speed.**

I. Introduction

THE microwave scattering characteristics of the ocean surface at moderate incidence angles appear to be largely explainable by composite surface scattering theory. This theory decomposes scattering surfaces into small-scale and large-scale features. The former are responsible for scattering directly while the latter provide low-frequency amplitude and phase modulation of the scattered signal. In this model, microwave scattering occurs because of resonant Bragg scattering from small-scale surface features in accordance with the equation:

$$\lambda_o = 2\lambda_B \cos\psi \tag{1}$$

where λ_o is the microwavelength, λ_B is the Bragg-resonant wavelength and ψ is the grazing angle.

The equation for the Doppler shift, F_D, due to a moving surface is

$$F_D = \frac{2C}{\lambda_o}\cos\psi = F_B \tag{2}$$

where C and F_B are the phase velocity and frequency of the Bragg-resonant waves.

The limitations of the composite model for the explanation of certain nonlinear features of microwave scattering are clear. Sea spikes, for example, are evident in moderate incidence angle measurements and may be associated with wave breaking [5], [6]. The difference between theoretical predictions and field measurements grow dramatically as grazing incidence is approached. Even 30 years ago differences in Doppler shift for vertical and horizontal polarizations of the scattered signal from a disturbed sea at grazing incidence for X, S, and L band radar [19] and C band radar [14] had been observed.

The physics of scattering at grazing incidence is poorly understood. The wind-wave tank studies reported here were conducted to better understand scattering at grazing incidence angles under repeatable wind and wave conditions. Traditional continuous wave (CW) scatterometers which are typically used for wave tank studies at moderate incidence angles do not satisfy the need for spatial resolution, with the more comprehensive wave tank studies [8]–[10] being restricted to minimum grazing angles of approximately 20°. A pulsed scatterometer is required in order to track scattering features in space and time. We are aware of only one such study at low grazing angles (7–10°) in a wind-wave tank [20], [21]. The authors used a dual-polarized, X-band scatterometer with good spatial resolution (10 cm) for studying the nature of sea spikes. Unfortunately, only the amplitude characteristics of the scattered signal were studied for an upwind direction of illumination and the special case of a wave field composed of long regular waves and short wind waves. It was proposed that non-Bragg scattering could explain the nature of the measured sea spikes.

The study reported here uses a dual-polarized, Ku-band, pulsed, Doppler scatterometer to measure the scattered signal for a wide range of wind and wave conditions and illumination geometry. Measurements of the scattering surface are made with wire wave gauges. In this paper we present results for scattering by wind waves only. A subsequent paper will present results for scattering by short waves in the presence of longer mechanically generated waves (or swell).

II. Experimental Methods

A. Wave Tank

Experiments were carried out in the large wind-wave channel at the Hydraulics Laboratory of the Scripps Institution

Manuscript received August 11, 1994; revised March 16, 1995. This research was supported in part by grants from ONR (Remote Sensing) and NSF (Physical Oceanography).

The authors are with Scripps Institution of Oceanography, University of California San Diego, La Jolla, CA 92093-0230 USA.

IEEE Log Number 9413198.

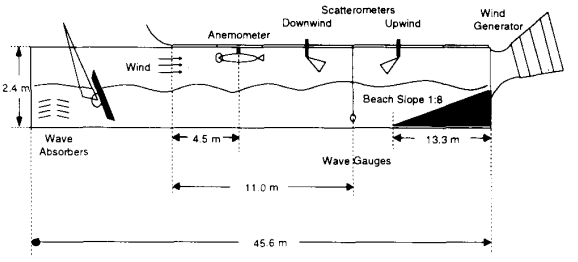

Fig. 1. A schematic of the wind-wave channel showing the respective locations of the scatterometer and environmental sensors.

of Oceanography (Fig. 1). This channel is 36 m long, 2.4 m wide, and 2.4 m in height with a water depth of 1.2 m. The scatterometer and wave gauges were mounted in the central glass-walled section of the channel. Winds from 2–12 m/s, measured by an anemometer 50 cm above the water surface, were generated using a fan which exhausted to the outside atmosphere 18 m downwind of the measurement site. A beach at the downwind end of the tank dissipated the waves. The height of the wind tunnel section of the tank was 1.2 m, the difference between the water depth and the full height of the channel. A fetch of 11 m from the entry section to the scattering footprint was used for all the measurements reported here.

B. Microwave System

A coherent, 14 GHz (2.1 cm), dual-polarized, pulsed system was used to obtain the amplitude and phase of the scattered signals. This system is adapted from a cw Ku-band scatterometer, which was designed and built by W. C. Keller at the US Naval Research Laboratory, Washington, DC and was used during the SAXON-CLT experiment [6].

The scatterometer is a two stage device consisting of high frequency (HF) and intermediate frequency (IF) stages (Fig. 2). The instrument uses two slightly different (ΔF = 240 MHz) transmitter frequencies to provide simultaneous vertical (VV) and horizontal (HH) polarized measurements. Two short-pulse modulators provided 2 ns-modulation to the transmitted signal. This phase-locked circuit synchronizes the repetition frequency of 3.75 KHz with the IF frequency of 240 MHz for reducing phase noise.

Energy transmitted from two local oscillators with slightly different frequencies is used to obtain IF conversion of the received vertical and horizontal polarized signals. The frequency of the received signal is 13.7 GHz or 13.94 GHz plus the Doppler frequency shift for vertical or horizontal polarization, respectively. The Doppler conversion is 94 Hz/ms^{-1}. After mixing for both polarizations the intermediate frequency signals with frequencies of 240 MHz plus Doppler shift are amplified in the HF unit and sent to the IF unit.

In the IF unit the intermediate frequency signals for both polarizations are split and shifted in phase by a quadrature hybrid device to produce two in-phase and two quadrature outputs. After a second mixing at IF = 240 MHz, four short-pulse video-frequency signals are obtained. A two-channel Stanford Research System Model SR250 Fast Gated Integrator and Boxcar Averager is used for converting the short-pulse signal with a bandwidth of 240 MHz to a low-frequency (0–3.75 KHz) analog signal. It could be connected to the in-phase outputs of the VV and HH channels, or to the in-phase and quadrature outputs of either channel; the output signals $e(t)$ are, respectively

$$e_1(t) = e_{VV}(t) \cdot \sin \Omega t; \quad e_2(t) = e_{HH}(t) \cdot \sin \Omega t \tag{3a}$$

or

$$e_1(t) = e_{VV}(t) \cdot \sin \Omega t; \quad e_2(t) = e_{VV}(t) \cdot \cos \Omega t \tag{3b}$$

or

$$e_1(t) = e_{HH}(t) \cdot \sin \Omega t; \quad e_2(t) = e_{HH}(t) \cdot \cos \Omega t \tag{3c}$$

where

$$\Omega = 2\pi F_D \tag{3d}$$

and e and F_D are the amplitude and Doppler shift of the scattered signal, respectively.

The transmitting and receiving antennas are two 20 cm diameter horns with a one-way, 3 dB beamwidth of approximately 6.7°. The antennas were mounted under the wind tunnel roof at a location 40–70 cm above the water surface and centered in the crosstank direction. The grazing angle could be varied from 6°to 12°, and could be positioned to give either an upwind or downwind direction of illumination.

The scatterometer was calibrated using a swinging 6.5 cm-diameter, aluminum sphere at a distance of 3.5 m, which was equal to the range to the center of the scattering footprint R. The R^{-4} range dependence was checked for $2 \leq R \leq 10$ m. The absolute mean cross section per unit area is then calculated according to

$$\sigma_0 = \frac{\sigma_s \langle e_w^2 \rangle}{\langle e_s^2 \rangle A_f} \tag{4a}$$

where $\langle e^2 \rangle = \langle e_1^2 + e_2^2 \rangle$ is the mean value of the squared output signal, defined by (3b) or (3c), for a signal scattered from surface waves, e_w, and from the sphere, e_s. Also, σ_s is the theoretical cross section of a perfectly conducting sphere, and A_f is the illuminated area of the antenna for the pulsed radar at grazing incidence, calculated according to

$$A_f = \frac{c(\tau_m + \tau_i)}{2} \cdot R\theta_c \cos \psi \tag{4b}$$

where θ_c is the antenna beamwidth in the crosstank-direction, c is the speed of light, and τ_m and τ_i are pulse widths for the modulator and gated integrator, respectively [$\tau_m \approx \tau_i$]. For R = 3.5 m, τ_m = 2 ns and τ_i = 3 ns, the size of the footprint was approximately 3000 cm^2. To insure an accurate determination of the footprint dimension, measurements were made with the calibrating sphere at a number of locations in both the crosstank and alongtank directions. The signal-to-noise ratio of the full system permitted the measurement of a minimum value of σ_o of −60 dB.

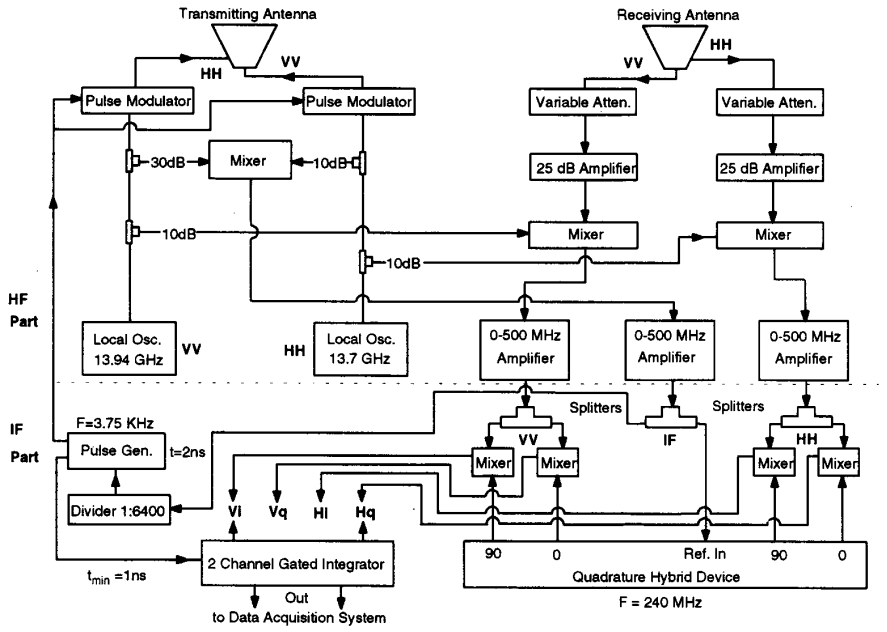

Fig. 2. Block diagram of the 14 GHz, 2.14 cm, dual-polarized, coherent, pulsed, Ku-band scatterometer.

C. Environmental Sensors

Resistance-type, 0.1 mm-diameter nichrome wire was used for the wave gauges. Two similar wave gauges were placed at the measurement site separated by 2.6 cm in the alongtank direction, but offset by 80 cm from the crosstank center position. A Kistler model 5004 41 dB amplifier (3 dB frequency response at 3 and 10 Hz) and a 20 dB Tektronics Model 107 amplifier (flat frequency response from 0–20 Hz) allowed measurement of the surface wave spectrum.

The change in frequency response of the wire wave gauge in the high frequency range due to capillary effects was measured by comparison with direct slope measurements made with a laser slope meter. It was found that the wire wave gauge response was essentially flat for frequencies less than 7 Hz, −3.6 dB at 10 Hz, and −12 dB at 20 Hz.

The centerline wind speed was measured 50 cm above the mean water level with a propeller-type Young model 05305 wind monitor which was calibrated with a Pitot-static tube. Air and water temperatures were measured with a standard mercury thermometer.

D. Data Acquisition and Processing

The computer used for data acquisition was a 486 PC equipped with two Metrabyte DAS16 cards (12 bit, 8 differential channel) for analog to digital conversion. Four analog signals (VV and HH scatterometer outputs and the wave gauge signals before and after filtering and amplification) were sampled at a frequency of 3.2 KHz (800 Hz per channel). Time series lengths were 1–2 minutes.

The main goal of this study was to understand the relationship between scattering and the geometry and kinematics of the water surface. This required simultaneous VV and HH measurements along with wave gauge data. Of particular interest are characteristics of the scattered signal and wave field such as Doppler spectra and phase velocity of the surface waves which could be associated with the motion of the scatterers. As will be shown below [Fig. 8(b) and (c)] the Doppler spectra are sufficiently narrow, and the frequency bands containing significant spectral density are well-separated from zero. This feature permitted using only one in-phase channel for computing the Doppler spectra. A comparison between Doppler spectra calculated using both in-phase and quadrature signals with spectra calculated using only the in-phase signal found them to be consistent. Therefore the amplitude (power) and phase (frequency) parameters of the scattered signal were defined separately, using only the in-phase components for VV and HH outputs [i.e., outputs in the form of (3a)].

1) Power: The signal in the form of (3a) was detected and high pass filtered at $F_c = 50$ Hz to remove phase fluctuations. The resulting magnitude (power envelope) was converted to a cross section per unit area σ_o using (4).

2) Frequency: To obtain the Doppler (phase) spectra of the signal corresponding to (3a), 2048 point FFT's were performed with a frequency resolution of 0.4 Hz. Note that the Doppler spectra include both frequency and amplitude fluctuations. A comparison with spectra of phase fluctuations only, obtained from the signal in the form of (3b) and (3c), was performed, and it was found that the influence of amplitude fluctuations is negligible in the frequency range considered.

The peak frequency F_o and 3 dB bandwidth ΔF of the smoothed Doppler spectra were determined in order to study their dependence on wave geometry and wind conditions.

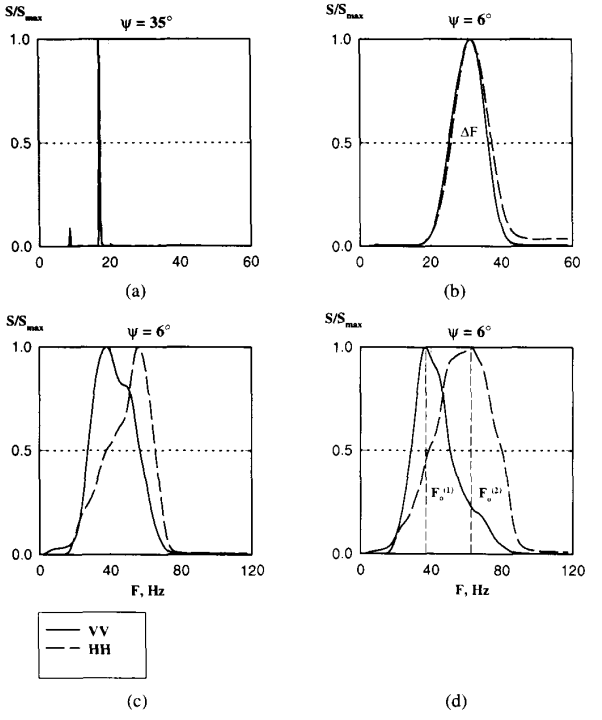

Fig. 3. Method of defining central frequency F_o and bandwidth ΔF of the Doppler spectra. Doppler spectra are smoothed and normalized by the maximum value of spectral density (a) $S/S_{\max}$ for quasiregular waves, (b) wind waves for $U = 2$ m/s, (c) $U = 4$ m/s, and (d) $U = 6$ m/s. F_o for the case of scattering from regular waves corresponds to Bragg scattering. F_o and ΔF increase with increasing wind. Note the appearance of a second non-Bragg peak in the spectra at higher wind speeds, especially for HH.

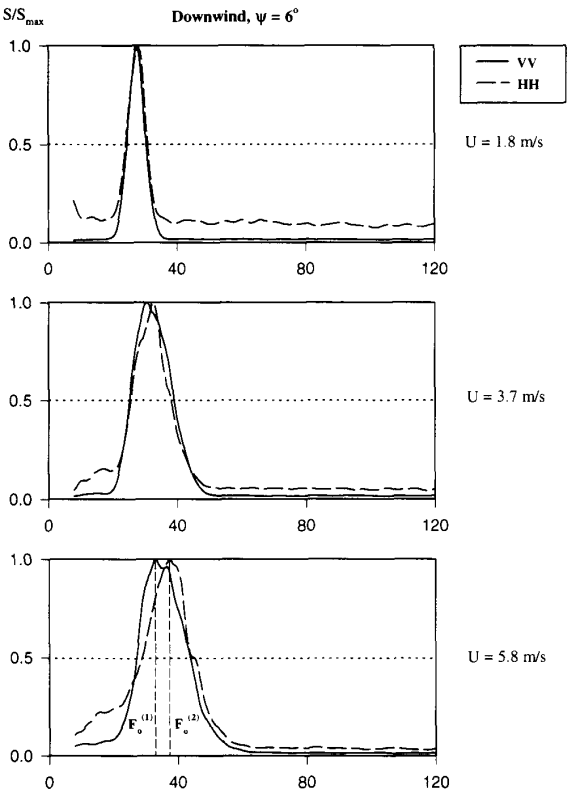

Fig. 4. Similar to Fig. 3 but for downwind illumination. Note the unimodal character of the Doppler spectra. The peak frequency F_o and bandwidth ΔF are approximately the same for vertical and horizontal polarization. Slight differences $[F_o^{(1)}/F_o^{(2)} = 1.1]$ can be observed for the highest wind speed, $U = 5.8$ m/s.

Consider, for example, the change in F_o and ΔF with increasing wind speed in Fig. 3. Doppler spectra for VV and HH polarizations are presented here which have been smoothed using an 8 Hz wide Bartlett window and normalized by the maximum value of the spectral density. Fig. 3(a) shows the Doppler spectra for a calibration experiment of scattering from quasiregular waves, produced by a high frequency mechanical wave generator, and demonstrates the frequency resolution of the whole system. A value of $F_o = 17.5$ Hz corresponds to that calculated by (2) for Bragg-scattering. The spectra for VV and HH are similar and very narrow. Their relative bandwidths $\Delta F/F_o = 0.03$ are close to the theoretical limit. A different picture can be seen for scattering by wind driven waves [Fig. 3(b)–(d)] for upwind illumination. The spectra are broad, values of F_o are shifted to higher frequencies, and differences between VV and HH polarizations become apparent with increasing wind speed. The central frequency F_o for VV polarization corresponds again to (2), including the effects of the wind drift velocity (6). Doppler spectra of both polarizations at higher wind speeds display some bimodal characteristics. While $F_o^{(1)}$ is dominant for VV, the higher frequency, $F_o^{(2)}$, appears dominant for the HH spectra. As will be shown later the higher peak $F_o^{(2)}$ may be associated with non-Bragg scattering from the more energetic wind waves.

The comparable results for downwind illumination are presented in Fig. 4. In this case, the peak frequency F_o and bandwidth ΔF of the unimodal Doppler spectra are approximately the same for both polarizations. The slight difference between F_o for HH and VV polarizations for the highest wind speed does not exceed 10%. As will be shown later, all cases can be associated with Bragg scattering.

3) Surface Waves: Wave-height spectra were calculated for all time series. To study features of the wave field at different wind conditions, the probability distributions of wave heights and slopes were calculated.

III. Results

A. Surface Waves

Fig. 5(a) shows typical wave height spectra for 10 different wind speeds in the range from 2–12 m/s. The peak frequency of the dominant waves decreases from 7 to 2 Hz with the increasing wind [Fig. 5(b)]; consequently, the wavelength increases from approximately 4 to 60 cm.

The comparison of this wave data with other data in the literature [8] shows that our wind-wave conditions are typical for wave tanks with similar dimensions. Some additional measurements using a Pitot-static tube for obtaining wind

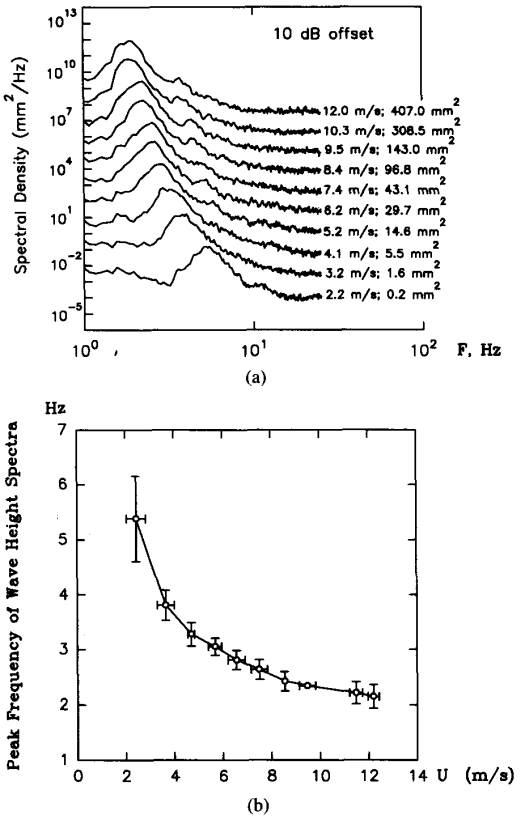

Fig. 5. Samples of wind wave parameters for different wind velocities. (a) Typical wave height spectra measured by the wave gauge. Each spectrum is offset by 10 dB. (b) Dependence of peak frequency of wave height spectra on wind speed.

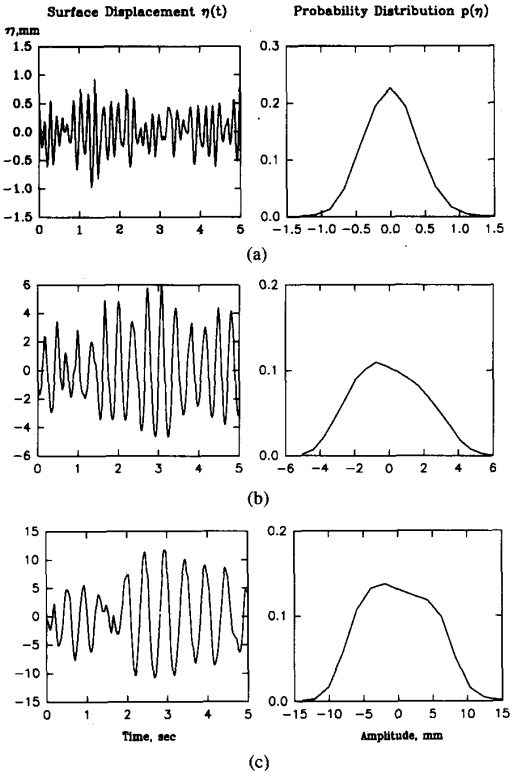

Fig. 6. The effect of increasing skewness of wave height $\eta(t)$ with increasing wind speed. Time series $\eta(t)$ (left) and its probability distribution $p(\eta)$ (right) for (a) $U = 2.9$ m/s, (b) $U = 5.3$ m/s, and (c) $U = 10.3$ m/s.

velocity as a function of height above the water surface confirmed this similarity. Thus, if necessary our wind data could be transformed into 19.5 m winds [8] or, as is more usual, friction velocity.

Direct measurement of the wind drift velocity, U_d, by observation of paper particles on the water surface showed that $U_d = (0.03 \pm 0.003)U$ for wind speeds less than 10 m/s where U is measured at 0.5 m.

In Fig. 6 three samples of surface displacement records $\eta(t)$ and their probability distributions for small, moderate, and large wind speeds are presented. Differences in the distribution of surface displacement is observed. It is clear that the skewness of the waves (sharper crests) increases with increasing wind speed.

Previous experiments [1], [9] have demonstrated upwind-downwind asymmetries in wind generated waves caused by the generation of parasitic capillary waves on the forward face of the longer wind waves, which may evolve into turbulent rollers [12] or microscale breaking. Such asymmetries may be responsible for the upwind-downwind differences we measured in the microwave scattering, so we undertook a separate series of measurements to confirm that similar asymmetries existed in our wave fields. Disturbances of larger wavenumber are accentuated by measuring the slope of the surface. In order to obtain a direct measurement of the wave slope (albeit relatively coarse), the surface displacement was simultaneously measured at two locations to give $\eta(x, t)$ and $\eta(x + \delta x, t)$, respectively, where $\delta x = 2.6$ cm. To improve the overall gain at the higher frequencies the time series were bandpass filtered at a central frequency of 7 Hz with 3 dB attenuation at 3 and 10 Hz. The measurements at the two locations were subtracted to give an estimate of the slope, $\mathcal{S}_x$

$$\mathcal{S}_x = \frac{\eta(x + \delta x, t) - \eta(x, t)}{\delta x}. \tag{5a}$$

An independent estimate of the slope, $\mathcal{S}_t$, was obtained by time differencing one of the time series with $\delta t = 0.015$ s, and using the phase speed C of the dominant waves to transform between temporal and spatial derivatives. Thus

$$\mathcal{S}_t = \frac{\eta(x, t + \delta t) - \eta(x, t)}{-C \cdot \delta t}. \tag{5b}$$

An example of these measurements for a wind speed of 6.2 m/s is shown in Fig. 7. In this case the effective spatial resolution of the temporal estimate of the slope is given by $\delta x = C \cdot \delta t = 0.9$ cm. The temporal and spatial estimates of the slope both show higher frequency waves ($F = 15$–20 Hz) near the crest of the dominant waves, with the amplitude of these disturbances being larger on the forward face of the dominant waves. Thus our data appear to be qualitatively consistent with the earlier measurements of high frequency

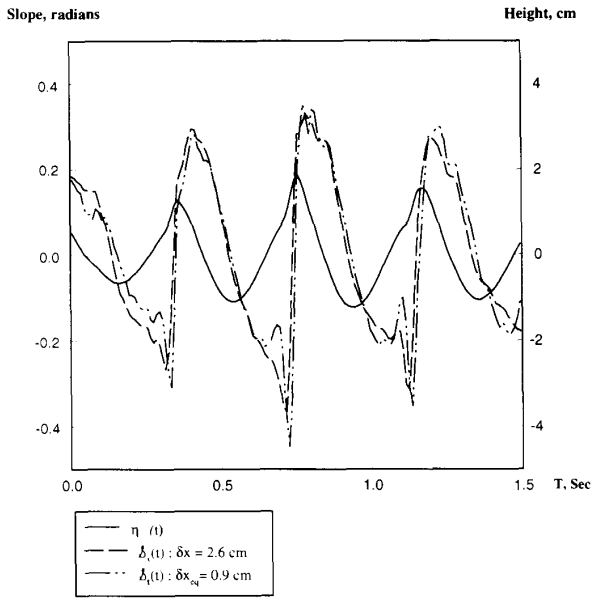

Fig. 7. A sample of bandpass filtered time series of wave height $\eta(t)$ and slopes $\mathcal{S}_x$ and $\mathcal{S}_t$ for $U = 6.2$ m/s. Note the presence of high frequency features ($F \approx 15$ Hz), especially on the front slopes of the dominant wind waves.

asymmetries cited above. Such disturbances may be a source of non-Bragg scattering as will be discussed below.[1]

B. Doppler Frequency

Fig. 8 presents several samples of Doppler spectra for the typical experiment at 6° grazing angle, for both upwind and downwind illumination. The wave height spectra for all values of wind speed from 1.8–11.4 m/s of this experiment are also shown. First we consider spectra for the downwind direction [Fig. 8(c)]. The sequence of spectra corresponds to wind increasing from bottom to top; each pair of VV and HH spectra are offset vertically for convenience. The peak frequency F_o and bandwidth ΔF of the Doppler spectra increase for both polarizations with the increasing wind.

One can see a different picture for the upwind direction [Fig. 8(b)]. The Doppler spectra show some evidence of a bimodal structure, with the energy of the second peak increasing with increasing wind (see spectra for 3.8 and 6 m/s). The first peak is dominant for all VV spectra and close to the corresponding value for the downwind direction. At the same time, the second peak for all HH Doppler spectra in the upwind direction is dominant except at the lowest wind speed. This polarization difference can be seen quite clearly in the dependence of the peak frequency of the Doppler spectra on wind speed.

Fig. 9 shows the peak frequency F_o as a function of wind speed for three values of grazing angle 6°, 8°, and 12°, and

[1] Since this paper was submitted, direct measurements of the slope profiles for several wind speeds have been made using a scanning laser slope gauge. Similar features to those presented in Fig. 7 which could clearly be associated with bound capillary waves were observed in greater detail than was possible with the wire wave gauges.

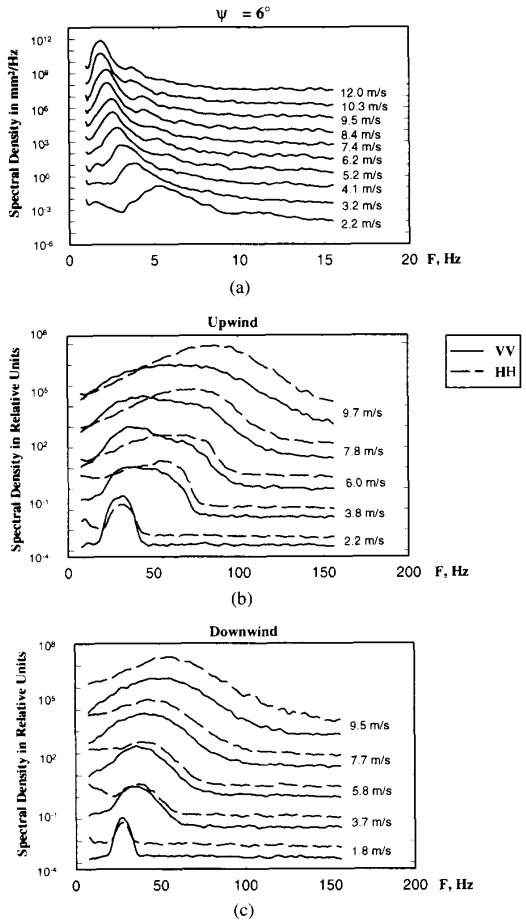

Fig. 8. Influence of the wind. (a) Smoothed wave height spectra for different wind speeds. Each spectrum is offset by 10 dB. (b) Smoothed VV and HH Doppler spectra for upwind illumination for different wind speeds. (c) Smoothed VV and HH Doppler spectra for downwind direction of illumination for different wind speeds. Each VV or HH spectrum is artificially offset by 14 dB from the previous spectrum. Note, the bimodal character of the upwind Doppler spectra for wind speeds from 3–8 m/s, especially for HH. The first peak may be associated with Bragg scattering, the second with scattering from steep waves near the peak of the spectrum.

for both the upwind and downwind directions of illumination. In all cases the peak frequency F_o increases with wind speed. Differences due to grazing angle are negligible while those due to polarization and direction of illumination are considerable. The dependence of F_o on wind falls into two compact groupings; Group I for HH with upwind illumination, and Group II for HH downwind and all VV. The values of F_o in Group I are noticeably larger.

The difference between these two groups is reinforced by measurements of bandwidth of Doppler spectra ΔF (Fig. 10). This parameter is associated with the coherence and decorrelation time of the scatterers and should therefore be useful in identifying these scatterers. The bandwidth ΔF increases approximately linearly with the wind for all the downwind and VV upwind data. The value of the relative bandwidth $\Delta F/F_o$ for the winds from 8–12 m/s is large (0.8–1) and may be evidence for considerable randomness of the scatterers.

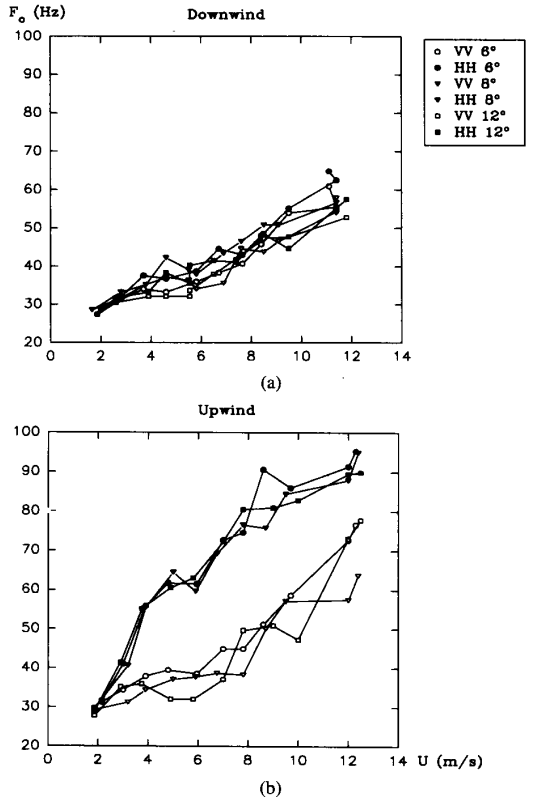

Fig. 9. Comparison of the peak frequencies of the Doppler spectra F_o versus wind speed for different polarizations and directions of illumination (a) downwind and (b) upwind.

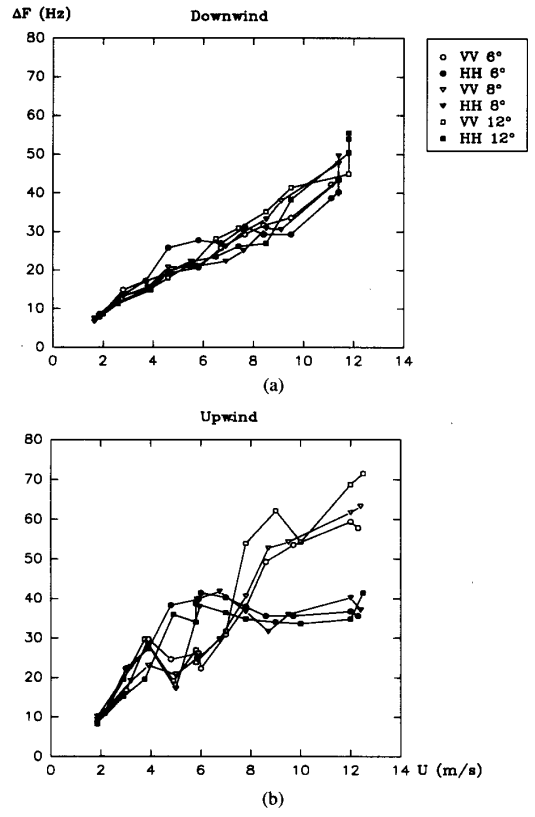

Fig. 10. Comparison of the absolute bandwidth ΔF versus wind speed for different polarizations and directions of illumination (a) downwind and (b) upwind.

At the same time the behavior of the curve $\Delta F(U)$ for the HH upwind direction is qualitatively different, becoming approximately constant after reaching a wind speed of 5–6 m/s. The normalized bandwidth $\Delta F/F_o$ (0.4–0.5) is also noticeably smaller.

C. Absolute Cross Section

The previous description of the Doppler characteristics suggests the presence of two (or perhaps more) different sources of scattering. The scattered power measured by absolute cross section might also show evidence of at least two different types of scatterers. Note, however, that the processing of the Doppler spectra emphasizes any difference present by selecting the spectral peak at a single frequency value whereas the absolute cross section processing involves the integration of the full spectra and therefore averages over the full range of frequency. Nevertheless a difference is again evident in the relationship between absolute cross section and wind.

Fig. 11 shows the dependence of the cross section σ_o on the wind speed U for three grazing angles and both upwind and downwind illumination. The similarity between both polarizations and the monotonic increase of σ_o with the wind speed for downwind illumination can be observed: σ_{VV} exceeds σ_{HH}, and the VV/HH polarization ratio is approximately 10–15 dB as expected.

However, Fig. 11(b) for upwind illumination displays some interesting features. The dependence of σ_{VV} on wind is comparable to that for downwind illumination. However, for HH, σ_o grows more rapidly for winds in the range 2–8 m/s before reaching values comparable to those for VV. Again, like the $F_o(U)$ and $\Delta F(U)$ data, (see Figs. 9 and 10) the σ_o data suggest the existence of a different scattering mechanism for HH polarization and upwind illumination.

It needs to be emphasized that the observed dependence of absolute cross section on wind speed exceeds in value the dependence of σ_o on different grazing angles. Fig. 12 shows the dependence on angle $\sigma_o(\psi)$ for both VV, HH and upwind and downwind illumination. For the three values of angle presented, the dependence of σ_o on ψ is demonstrated to be less than that for σ_o on U.

IV. Discussion

This study of the amplitude and frequency characteristics of microwave scattering for different polarizations and directions of illumination distinguishes two separate groupings of the backscattered data. The first grouping corresponds to HH scattering in the upwind look direction and the second grouping corresponds to HH scattering in the downwind look direction and all VV. These groups may be associated with different scattering mechanisms. The second grouping is considered to

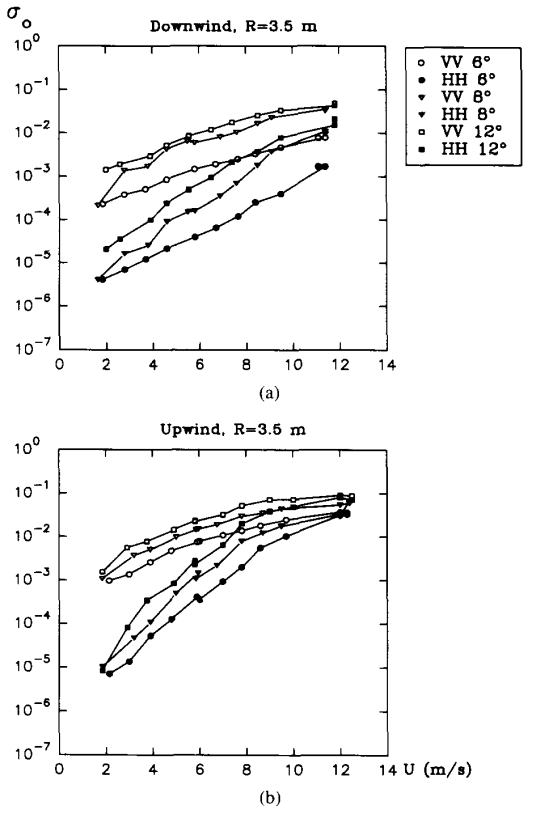

Fig. 11. Comparison of the mean cross section per unit area σ_o versus wind speed for different polarizations and directions of illumination (a) downwind and (b) upwind.

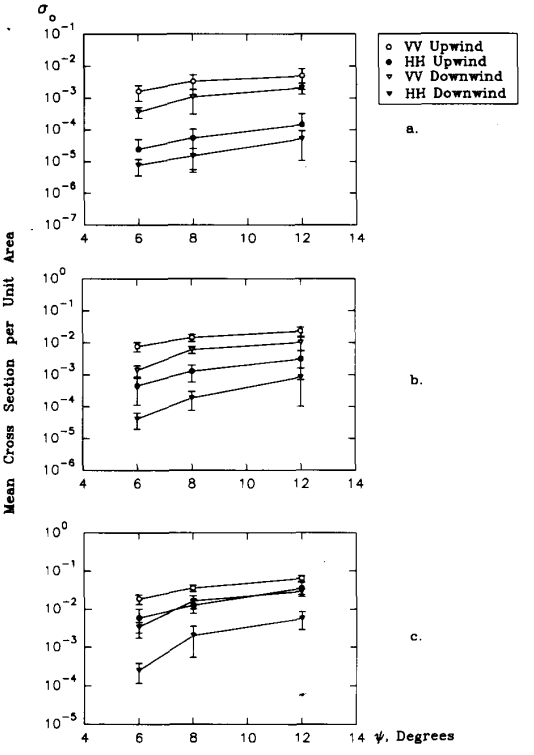

Fig. 12. Dependence of the mean cross section per unit area σ_o on grazing angle ψ for (a) small wind U = 2–4 m/s, (b) moderate wind U = 5–7 m/s, and (c) large wind U = 8–10 m/s.

be associated with Bragg scattering from small capillary wind waves while the first is interpreted as non-Bragg scattering from the dominant gravity wind waves. We shall attempt to demonstrate that such a separation is consistent with estimates of the phase velocities of the different types of wind waves.

Fig. 13 presents the wind-wave phase velocity as a function of wind speed as determined by calculation, and by converting the Doppler shift frequencies from the backscattered signals to phase velocity.

The calculation of phase velocity was made according to:

$$C = C_o + \alpha \cdot U_d; \quad U_d = 0.03U \tag{6}$$

where $U_d = 0.03U$ is the wind drift current at the water surface, α is a numerical coefficient, and C_o is the phase velocity based on the dispersion relation for gravity-capillary waves

$$C_o = \frac{\omega}{k} = \sqrt{\frac{g}{k} + \frac{Tk}{\rho}}. \tag{7}$$

Here, ω is the angular frequency of the surface waves, taken from the peak frequency for the steep wind waves or Bragg resonant frequency for the capillary waves, k is the wave number of the surface waves, g is the acceleration of gravity, T is surface tension, and ρ is the water density.

The coefficient α in the correction for the wind-drift is a factor of the velocity profile in the water column and the frequency or wave number of the surface waves. However, the departure from a constant value of unity is only small for the range of parameters in these results [3]. Including the dependence of α on k is estimated to lead to improvements of less than 10% in the correction to C.

For the measurement of phase velocity, the peak frequency of the Doppler spectrum is converted to velocity using the Doppler conversion of 94 Hz per m/s for both dominant (Group I) and Bragg-component wind waves (Group II).

We first compare the results for Group I. There is good agreement for both the measured data (curve 2) and the calculated data (curve 1) for wind speeds less than 8–9 m/s. Some of the difference between the measured and calculated Doppler shift may be explained by the influence of the finite size of the antenna footprint [18]. Recall that the measured Doppler data for Group I corresponds to the case of HH upwind.

Now we consider Group II. Using the Doppler scatterometer for the measurement of phase velocity for the Bragg-component capillary waves (wavelength approximately 1 cm) is a well known procedure [16] for longer wavelengths. For Group II, the Doppler measurement is taken from the average of HH downwind and both VV illuminations. The results of the Doppler measurement (curve 3) and calculation by (7) (curve 4) of the phase velocity of Bragg-component capillary

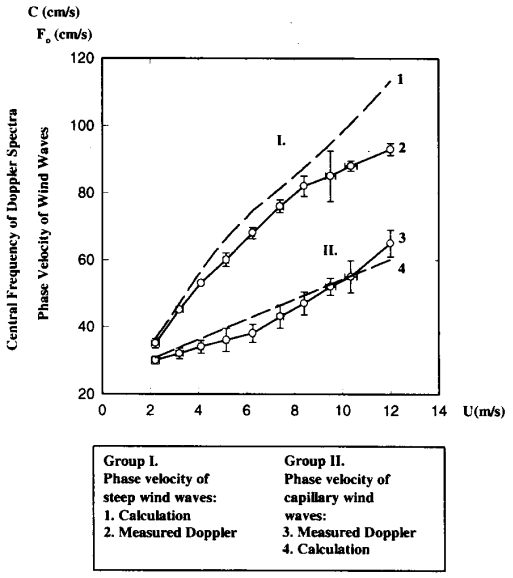

Fig. 13. Comparison of different types of scatterers and dependence of different scatterers on wind speed. Group I: Phase velocity of energy containing wind waves: Curve 1—calculated by (6) for dominant wind waves. Curve 2–HH upwind Doppler spectra measurements. Group II: Phase velocity of free Bragg component with $\lambda = 1$ cm: Curve 3—HH downwind and all VV Doppler spectra measurements (mean values). Curve 4—calculated by (6) for free Bragg component wind waves.

wind waves show good agreement. Thus the phase velocity measurements give additional evidence of the different nature of the scattering mechanism of Group I and Group II.

We now attempt to identify the location of the Group I non-Bragg scatterers.[2] There has been much speculation in the past about the nature and location of such scatterers. In a time-domain model (for a ultra-high resolution scatterometer) [23], the sensitivity of the scattered signal to both the curvature and slope of the scattering surface was mentioned. Reference [21] found qualitative agreement with this model. Using an X-band coherent scatterometer with ultra-high spatial resolution at grazing incidence angles in a laboratory wind-wave tank, they made deterministic comparisons of synchronous scatterometer and scanning laser slope gauge signals. Two groups of spiky signals were observed for HH upwind scattering with low Doppler frequency on the troughs of 1-s long mechanically generated waves, and high peak Doppler frequency on the crests.

We cannot use a deterministic interpretation like [21] because of our different spatial resolutions; with our pulselengh of 75 cm corresponding to several (2–12) dominant wavelengths for the different wind speeds.

Reference [14] explained the difference in HH and VV mean Doppler shift during a C-band field experiment as being due to the different penetration depths for different polarizations. A similar difference in HH and VV mean Doppler shifts in X-, L-, and S-band field measurements of [19] were observed. They explained the polarization difference by a surface model composed of Bragg scattering with a shadowing factor due to the presence of long and steep waves [11]. The shadowing by the long waves is a crucial factor in the interpretation by [14], [19] and therefore should be extended to our present study. Surprisingly the effect of shadowing of the surface is negligible in our measurements. Some additional measurements for both directions of illumination and grazing angles up to 28″ [17] do not demonstrate any significant differences in the Doppler peak values for grazing angles from 6–28° for all wind conditions. Therefore we can exclude effects related to shadowing.

Reference [20] used the following four scattering models for comparison with the measured VV/HH ratio: 1) a specular scatter model, used by [5]; 2) a spray model; 3) a wedge model [13]; and 4) a spilling breaker model . Furthermore, [10] proposed a model of gently breaking waves.

We can exclude from consideration the first two models due to the small grazing angles 1) and the lack of spray 2) in our tank. The large difference in the value of σ_o between the upwind and downwind directions of illumination (approximately 10 dB at the higher wind speeds) indicates the small effect of wedge scattering. Furthermore, non-Bragg scattering for HH in the upwind direction under moderate wind conditions is apparent without any visible indication of significant breaking. This is motivation for seeking some additional wave effects as a source of scattering. A sample of such a wave feature was shown in Fig. 7. Similar features of wind wave slopes were observed by [10] using a scanning laser slope gauge. The authors identified them as patches with parasitic capillary waves due to gentle breaking. The second peak in the Doppler spectra appeared under these conditions in their measurements: VV and HH, X-band, CW-scatterometer, upwind direction of illumination at 55° incidence angle and wind speed 7.9 m/s. One should note that the presence of such patches in the wave slope time series are visible for all values of wind above 3–4 m/s. References [2], [4] have also noticed the appearance of such high gradient patches under similar conditions in a wind-wave basin.

[2]By "non-Bragg" in this paper we mean scatterers which do not satisfy both the Bragg resonance condition *and* the free surface wave dispersion relationship. This does not exclude bound scatterers satisfying only the (spatial) Bragg resonance condition.

ACKNOWLEDGMENT

The authors wish to thank C. Coughran and colleagues at the Hydraulics Laboratory, Scripps Institution of Oceanography for technical support and unflagging assistance in the experiments. They thank the anonymous reviewers for their helpful comments on the original version of this paper.

REFERENCES

[1] C. S. Cox, "Measurements of slopes of high frequency wind waves," *J. Marine Research,* pp. 199–230, 1958.
[2] N. Ebuchi, H. Kawamura, and Y. Toba, "Physical processes of microwave backscattering from laboratory wind wave surfaces," *J. Geophys. Res.*, vol. 98, no. C8, pp. 14669–14681, 1993.
[3] V. V. Goncharov and I. A. Leykin, "Waves on a current with velocity shear," *Oceanol. Acad. Sci. USSR,* vol. 23, no. 2, pp. 155–159, 1983.
[4] N. E. Huang and S. R. Long, "An experimental study of the surface elevation probability distribution and statistics of wind-generated waves," *J. Fluid Mechanics,* vol. 101, no. 1, pp. 179–200, 1980.
[5] A. T. Jessup, W. C. Keller, and W. K. Melville, "Measurements of sea spikes in microwave backscatter at moderate incidence," *J. Geophys. Res.*, vol. 95, no. C6, pp. 9679–9688, 1990.

[6] ——, "Breaking waves affecting microwave backscatter," *J. Geophys. Res.*, vol. 96, no. C11, pp. 20547–20569, 1991.
[7] W. C. Keller and J. W. Wright, "Microwave scattering and the straining of wind generated waves," *Radio Sci.*, vol. 10, no. 2, pp. 139–147, 1975.
[8] M. K. Keller, W. C. Keller, and W. J. Plant, "A wave tank study of the dependence of X band cross sections on wind speed and water temperature," *J. Geophys. Res.*, vol. 97, no. C4, pp. 5771–5792, 1992.
[9] D. S. W. Kwoh and B. M. Lake, "A deterministic, coherent, and dual polarized laboratory study of microwave backscattering from water waves, Part I: Short gravity waves without wind," *IEEE J. Oceanic Eng.*, vol. 9, no. 5, pp. 291–308, 1984.
[10] ——, "The nature of microwave backscattering from water waves," *Ocean Surface*, pp. 249–256, 1985.
[11] I. A. Leykin, I. E. Ostrovsky, A. D. Rozenberg, V. G. Ruskewich, and I. M. Fooks, "Effects of long waves on the energy spectra of radio signals scattered by the surface of the sea," *Izv. Vuzov Radiofizika*, vol. 18, no. 3, pp. 247–254, 1975.
[12] M. S. Longuet-Higgins, "Capillary rollers and bores," in M. L. Banner and R. H. J. Grimshaw, Eds., *Breaking Waves*. Berlin: Springer-Verlag, 1992, pp. 21–37.
[13] D. R. Lyzenga, A. L. Maffett, and R. A. Shuchman, "The contribution of wedge scattering to the radar cross section of the ocean surface," *IEEE Trans. Geosci. Remote Sensing*, vol. 21, pp. 502–505, July 1983.
[14] V. W. Pidgeon, "Doppler dependence of radar sea return," *J. Geophys. Res.*, vol. 73, no. 4, pp. 1333–1341, 1968.
[15] W. J. Plant and W. C. Keller, "Evidence of Bragg scattering in microwave doppler spectra of sea return," *J. Geophys. Res.*, vol. 95, no. C9, pp. 16,299–16,310, 1990.
[16] W. J. Plant and J. W. Wright, "Phase speeds of upwind and downwind traveling short gravity waves," *J. Geophys. Res.*, vol. 85, no. C6, pp. 3304–3310, 1980.
[17] A. D. Rozenberg, D. C. Quigley, and W. K. Melville, "Laboratory study of polarized scattering at grazing incidence: The influence of long waves," *IEEE Trans. Geosci. Remote Sensing*, to appear.
[18] A. D. Rozenberg, "Measurements of modulation transfer function sea surface-backscattered signal at 3 cm wavelength," *Izv. Vuzov Radiofizika*, vol. 33, no. 1, pp. 1–8, 1990.
[19] A. D. Rozenberg, I. E. Ostrovskii, and A. I. Kalmykov, "Frequency shift of radiation scattered from a rough sea surface," *Izv. Vuzov Radiofizika*, vol. 8, no. 6, pp. 234–240, 1966.
[20] D. B. Trizna, J. P. Hansen, P. Huang, and J. Wu, "Laboratory studies of radar sea spikes at low grazing angles," *J. Geophys. Res.*, vol. 96, no. C7, pp. 12529–12537, 1991.
[21] ——, "Ultra-wideband radar studies of steep crested waves with scanning laser measurements of wave slope profiles," *Dynamics Atmosph. Oceans*, vol. 20, pp. 33–53, 1993.
[22] L. B. Wetzel, "A model for sea backscatter intermittency at extreme grazing angles," *Radio Sci.*, vol. 12, no. 5, pp. 749–756, 1977.
[23] ——, "A time domain model for sea scatter," *Radio Science*, vol. 28, no. 2, pp. 139–150, 1993.

Anatol D. Rozenberg received the Ph.D. degree in radio engineering from the Institute of Radiophysics and Electronics, Ukrainen Academy of Sciences, USSR and the D.Sc. degree in physics and mathematics from the P. P. Shirshov Institute of Oceanology, USSR Academy of Sciences, both in 1982.

He is now with the Marine Physical Laboratory of the Scripps Institution of Oceanography where his major research interests include experimental study of microwave scattering from rough water surfaces with application to remote sensing.

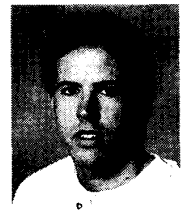

Derek C. Quigley received the B.S. degree in physics at the University of California, San Diego in 1993.

Since 1993, he has been a Research Associate at the Scripps Institution of Oceanography working on problems in acoustic and microwave remote sensing for investigation of surface wave field parameters.

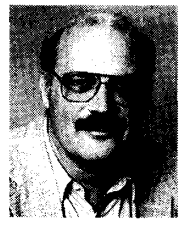

W. Kendall Melville received a B.Sc. degree in applied mathematics, and B.E. and M.Eng.Sc. degrees in aeronautical engineering at the University of Sydney, Sydney, Australia, and the Ph.D. degree in aeronautics and astronautics at the University of Southampton.

In 1977, he became a Researcher at the Institute of Geophysics and Planetary Physics, UCSD, and in 1980 a Professor at the Massachusetts Institute of Technology. In 1991, he returned to UCSD as a Professor of Oceanography at the Scripps Institution of Oceanography. His research interests include fluid mechanics, ocean waves, air-sea interaction, acoustical oceanography, and microwave remote sensing of the sea surface.

Dr. Melville was awarded a Guggenheim Memorial Fellowship in 1986.